

Depth-variant maximum-likelihood restoration for three-dimensional fluorescence microscopy

Chrysanthe Preza

*Department of Electrical Engineering, Washington University, St. Louis, Missouri
63130*

José-Angel Conchello

*Program in Molecular and Cell Biology, Oklahoma Medical Research Foundation,
and Program in Biomedical Engineering, Chemical Engineering Dept., University of
Oklahoma, Norman, Oklahoma 73019*

We derive an algorithm for maximum-likelihood image estimation based on the expectation maximization (EM) formalism using a new approximate model for depth-varying image formation for optical-sectioning microscopy. This new strata-based model incorporates spherical aberration that worsens as the microscope is focused deeper under the cover slip and is the result of the refractive index mismatch between the immersion medium and the mounting medium of the specimen. Images of a specimen with known geometry and refractive index show that the model captures the main features of the image. We analyze the performance of the depth-variant EM (DV-EM) algorithm with simulations, which show that the algorithm can compensate for image degradation changing with depth.

© 2003 Optical Society of America

OCIS codes: 100.3020, 100.3190, 100.6890, 170.6900, 180.2520, 180.6900,

999.9999 depth-variant imaging model, maximum-likelihood estimation

1. Introduction

Three-dimensional (3D) fluorescence microscopy via the method of computational optical sectioning is a very powerful technique for the visualization of thick biological specimens. In computational optical sectioning microscopy (COSM), the resolution and contrast of the 3D images are improved by computational processing. Several different model-based algorithms for COSM have been derived by us¹⁻⁷ and by others.⁸⁻¹⁸ The goal of these algorithms is to estimate the specimen function (e.g. the concentration of fluorescent dye) given the recorded image, a mathematical model for the process of image formation and recording, and any known information about the specimen. To keep the computational load practical, simplifying assumptions are made in the derivation of the model. Different assumptions as well as different approaches for the inversion of the imaging process result in different algorithms. In general, algorithms based on more accurate models yield better results, but they are also more computationally demanding.

Two simplifying assumptions common to most (if not all) existing algorithms for COSM are linearity and space-invariance. Linearity is a reasonable approximation when the vast majority of the photons emitted from a point in the specimen do not interact with other portions of the specimen before being collected by the objective lens. Space invariance is a reasonable approximation when the point spread function (PSF) of the microscope—the image of a point source of light, does not change sig-

nificantly over the 3D field of view. When image formation can be approximated as being linear and space invariant, the forward model is a 3D convolution that can be evaluated using fast Fourier transforms (FFTs). For thick biological specimens, however, space invariance does not necessarily hold. This is because of refraction due to variations in the specimen's refractive index^{19,20} and also because of aberrations due to the increasing imaging depth.²¹ Microscope objectives are designed to be free of aberrations only for a plane immediately below the cover slip. Obviously, only the top-most layer of the specimen is immediately beneath the cover slip whereas focusing the microscope at other depths under the cover slip introduces spherical aberration (SA)²¹ (see Figure 1). The amount of SA introduced increases with three factors: 1) the depth under the cover slip at which the microscope is focused; 2) the degree to which the refractive index in the specimen mounting medium differs from the refractive indices of the immersion medium and cover slip; and 3) the numerical aperture (NA) of the objective lens. Although there are objectives that can be adjusted to eliminate SA at arbitrary depths under the cover slip, they are free of SA only at the depth for which they are adjusted. Focusing the microscope at planes in the specimen above and below this depth introduces SA. Thus, portions of the specimen above and below this depth are imaged with a spherically-aberrant PSF. More recently, methods have been developed that dynamically compensate for the depth-induced SA as the microscope is focused at different depths.²²⁻²⁵ These methods are based on using deformable mirrors to counteract the phase error caused by the depth under the cover slip. At this time, however, such methods are still under development.

Most biological specimens are mounted on an aqueous medium (either water or

saline solution) with a refractive index of approximately 1.33. For the high NA objectives ($NA > 1.0$) necessary for high resolution, the refractive index of the immersion oil and the cover slip is either $n = 1.515$ for objectives with NA up to approximately 1.4 or $n = 1.8$ for newer objectives with $NA = 1.65$. The large mismatch in the refractive index of the mounting medium relative to that of the immersion medium and cover slip not only introduces a significant amount of SA but also causes the amount of SA to change significantly with increasing depth under the cover slip at which the microscope is focused.^{21, 26-28} In these cases, space-invariance is no longer a reasonable assumption and the forward model can no longer be approximated by a convolution. Therefore, estimating the specimen function assuming space-invariance produces artifactual estimated images. Unfortunately, the space-varying model of image formation results in a forward model with a very high computational complexity in terms of CPU time and memory. Thus, a reasonable approximation to the space-varying image formation is necessary. In this article, we present such an approximation and derive a maximum-likelihood (ML) image estimation algorithm based on the expectation-maximization (EM) formalism of Dempster, Laird, and Rubin.²⁹ This algorithm can be applied to different fluorescence microscope modalities such as wide-field, confocal scanning, and two-photon fluorescence excitation. The imaging model we derived does not include the effects of light-scattering and assumes that refractive index variations throughout the specimen are negligible. With these assumptions, the PSF varies only with the depth under the cover slip at which the microscope is focused.

If the PSF does not change very rapidly with depth, then it is possible to approximate the forward model using a small number of PSFs, each computed at a

different depth by allowing a variable number of neighboring pixels to be associated with the same PSF or with the interpolation of two PSFs. Similar approaches that approximate space-variant estimation problems have been reported for astronomical imaging^{32–34} and for other applications.^{35,36}

The paper is organized as follows. In Section 2, we present an approximate model for depth-varying image formation for fluorescence microscopy. In Section 3, we present the derivation of a new EM-based restoration algorithm for depth-varying imaging (which we denote by DV-EM) based on the approximate model presented in Section 2. Section 4 describes simulations for the evaluation of the model and the restoration algorithm. In Section 5, we present results obtained with simulations and compare them with results obtained with the EM algorithm from a space-invariant image formation model (available in our XCOSM v2.5 package³¹). We conclude the paper in Section 6 with a discussion of the results we present here.

2. Depth-variant stratum-based imaging model

For a 3D PSF that varies only with the depth z_i at which the microscope is focused, the image recorded at $\mathbf{x}_i \in \mathcal{I}$ can be represented by the superposition integral

$$g(\mathbf{x}_i) = \int_{\mathcal{O}} h(\mathbf{r}_i - \mathbf{r}_o, z_i, z_o) s(\mathbf{x}_o) d\mathbf{x}_o. \quad (1)$$

where $\mathbf{x}_i = (x_i, y_i, z_i)$ and $\mathbf{r}_i = (x_i, y_i)$ are a 3D and a two-dimensional (2D) point, respectively, in image space \mathcal{I} ; $\mathbf{x}_o = (x_o, y_o, z_o)$ and $\mathbf{r}_o = (x_o, y_o)$ are a 3D and a 2D point, respectively, in object space \mathcal{O} ; $s(\mathbf{x}_o)$ is the specimen function, i.e. the concentration of fluorescent dye at $\mathbf{x}_o \in \mathcal{O}$; and $h(\mathbf{r}_i - \mathbf{r}_o, z_i, z_o)$ is the depth-varying

PSF, i.e. the intensity of light at pixel \mathbf{r}_i produced by an incoherent point source at (\mathbf{r}_o, z_o) when the microscope is focused at a plane conjugate to z_i .

In a restoration algorithm, the forward model given by Eq. (1) is evaluated in discrete form to yield an estimated sampled image. Numerical evaluation of Eq. (1) requires storing a 4D array $h(\mathbf{r}_o, z_i, z_o)$ because a different 3D PSF is needed for each plane in the image. Furthermore, the evaluation of Eq.(1) requires a large number of 2D convolutions—one for each pair of depths (z_i, z_o) . A reduction of the number of PSFs needed to evaluate Eq. (1) can be made by allowing a variable number of neighboring pixels to be associated with the same PSF.³² If the PSF does not change very rapidly with depth z_i , then it is possible to approximate Eq. (1) using a small number of PSFs, each computed at a different depth $z_i = Z_m$, $m = 1, 2, 3, \dots, M$. This approximation is similar to the one proposed by Trussell and Hunt³⁵ and used by Boden, et al. for astronomical imaging.³³ In our first approach of sectioning the image restoration problem presented in Ref. 37 we partitioned the object space \mathcal{O} into M non-overlapping strata, centered at depths $z_i = Z_m$, $m = 1, 2, 3, \dots, M$ and used an overlap-add method for block convolution³⁸ to approximate Eq. (1). This approach is inherently stratified and yields results that are not continuous from one stratum to the next. To ameliorate this problem we now approximate Eq. (1) by interpolating between adjacent strata.

In our new stratum-based model, we partition the object space \mathcal{O} into M non-overlapping strata,

$$\mathcal{O}_m = \{\mathbf{x}_o = (x_o, y_o, z_o) : Z_m \leq z_o < Z_{m+1}\}; \quad m = 1, 2, 3, \dots, M$$

where $z_o = Z_m$ and $z_o = Z_{m+1}$ are the upper and lower boundaries respectively of the m -th stratum and M is the number of strata. The object is the superposition

$$s(\mathbf{x}_o) = \sum_{m=1}^M s_m(\mathbf{x}_o), \quad (2)$$

where

$$s_m(\mathbf{x}_o) = \begin{cases} s(\mathbf{x}_o) & \text{for } \mathbf{x}_o \in \mathcal{O}_m \\ 0 & \text{otherwise.} \end{cases}$$

The thickness of each stratum is chosen such that the PSF does not change significantly throughout the stratum. Thus, if we define a sequence of $M + 1$ PSFs at depths $z_i = Z_m$ as

$$h_m(\mathbf{x}_o) = h(\mathbf{r}_o, Z_m, z_o) \quad m = 1, 2, 3, \dots, M + 1, \quad (3)$$

the PSF associated with stratum $s_m(\mathbf{x}_o)$ is the interpolation of the PSFs at depths $z_i = Z_m$ and $z_i = Z_{m+1}$ given by:

$$\tilde{h}_m(\mathbf{x}_i, \mathbf{x}_o) = a_m(z_o)h_m(\mathbf{x}_i - \mathbf{x}_o) + [1 - a_m(z_o)]h_{m+1}(\mathbf{x}_i - \mathbf{x}_o), \quad (4)$$

where

$$a_m(z_o) = \begin{cases} \frac{Z_{m+1} - z_o}{Z_{m+1} - Z_m} & \text{for } z_o \in \mathcal{O}_m \\ 0 & \text{otherwise.} \end{cases}$$

We approximate the image of a stratum $s_m(\mathbf{x}_o)$ as

$$g_m(\mathbf{x}_i) = \int_{\mathcal{O}} \tilde{h}_m(\mathbf{x}_i, \mathbf{x}_o) s_m(\mathbf{x}_o) d\mathbf{x}_o \quad m = 1, 2, 3, \dots, M \quad (5)$$

and the image of the object by the sum of all the strata images:

$$g(\mathbf{x}_i) \approx \sum_{i=1}^M g_m(\mathbf{x}_i), \quad (6)$$

which requires the computation of $2M$ 3D convolutions. This approximation improves as the number of PSFs (or, equivalently, the number of strata) increases and is exact when each stratum has only one plane. However, increasing the number of strata increases the computation time and the memory requirements of the algorithm.

3. Restoration Algorithm

The EM algorithm for ML estimation based on Poisson statistics²⁹ has been adapted by us and others to optical sectioning microscopy for a space-invariant imaging model.^{5,6,12,15,16,30,39} Using Eq. (6) to approximate the depth-variant imaging model we have derived a new algorithm for ML optical sectioning microscopy based on the EM formalism.

Following the EM formalism in Ref. 40, we define the complete data set as $N(d\mathbf{x}_i, d\mathbf{x}_o)$, the number of photons emitted from $[\mathbf{x}_o, \mathbf{x}_o + d\mathbf{x}_o) \subset \mathcal{O}$ and detected at $[\mathbf{x}_i, \mathbf{x}_i + d\mathbf{x}_i) \subset \mathcal{I}$. For a given pair of points $(\mathbf{x}_i, \mathbf{x}_o)$, $N(d\mathbf{x}_i, d\mathbf{x}_o)$ follows a Poisson distribution with mean

$$\mu(d\mathbf{x}_i, d\mathbf{x}_o) = \begin{cases} \tilde{h}_m(\mathbf{x}_i - \mathbf{x}_o)s_m(\mathbf{x}_o)d\mathbf{x}_i d\mathbf{x}_o & \text{for } \mathbf{x}_o \in \mathcal{O}_m \\ 0 & \text{otherwise.} \end{cases}$$

The log-likelihood of the complete data set is given by

$$\mathcal{L}_{cd} = - \int_{\mathcal{I}} \int_{\mathcal{O}} \mu(d\mathbf{x}_i, d\mathbf{x}_o) + \int_{\mathcal{I}} \int_{\mathcal{O}} \ln[s(\mathbf{x}_o)]N(d\mathbf{x}_i, d\mathbf{x}_o), \quad (7)$$

where terms independent of $s(\mathbf{x}_o)$ were dropped. The expectation of Eq. (7) conditioned on the estimate at iteration (k) , $\hat{s}^{(k)}(\mathbf{x}_o)$, and the recorded data $g(\mathbf{x}_i)$ modeled

by Eq. 6 is given by

$$\begin{aligned}
Q[s|\hat{s}^{(k)}] &= - \int_{\mathcal{O}} \sum_m s_m(\mathbf{x}_o) \int_{\mathcal{I}} \tilde{h}_m(\mathbf{x}_i - \mathbf{x}_o) d\mathbf{x}_i d\mathbf{x}_o \\
&\quad + \int_{\mathcal{O}} \ln[s(\mathbf{x}_o)] \sum_m \hat{s}_m^{(k)}(\mathbf{x}_o) \int_{\mathcal{I}} \tilde{h}_m(\mathbf{x}_i - \mathbf{x}_o) \frac{g(\mathbf{x}_i)}{\hat{g}^{(k)}(\mathbf{x}_i)} d\mathbf{x}_i d\mathbf{x}_o, \quad (8)
\end{aligned}$$

where $\hat{g}^{(k)}(\mathbf{x}_i)$ is the image of $\hat{s}^{(k)}(\mathbf{x}_o)$ obtained from the stratum-based model (Eqs. (6) and (5)). In the maximization step of the EM formalism, an estimate of $s(\mathbf{x}_o)$ is computed to maximize Eq. (8), i.e.,

$$\begin{aligned}
\hat{s}^{(k+1)}(\mathbf{x}_o) &= \operatorname{argmax} Q[s|\hat{s}^{(k)}], \quad (9) \\
s(\mathbf{x}_o) &\geq 0
\end{aligned}$$

which gives

$$\hat{s}_m^{(k+1)}(\mathbf{x}_o) = \frac{1}{H_M(z_o)} \hat{s}_m^{(k)}(\mathbf{x}_o) \int_{\mathcal{I}} \tilde{h}_m(\mathbf{x}_i - \mathbf{x}_o) \frac{g(\mathbf{x}_i)}{\hat{g}^{(k)}(\mathbf{x}_i)} d\mathbf{x}_i, \quad \text{for } \mathbf{x}_o \in \mathcal{O}_m \quad (10)$$

for $m = 1, \dots, M$, where

$$H_M(z_o) = \sum_m \{a_m(z_o) H_m + [1 - a_m(z_o)] H_{m+1}\}$$

and

$$H_m = \int_{\mathcal{I}} h_m(\mathbf{x}_i - \mathbf{x}_o) d\mathbf{x}_i.$$

We write the estimate as the interpolation of two convolution integrals by substituting

Eq. (4) in Eq. (10):

$$\begin{aligned}
\hat{s}^{(k+1)}(\mathbf{x}_o) &= \frac{\hat{s}^{(k)}(\mathbf{x}_o)}{H_M(z_o)} \left\{ a_m(z_o) \int_{\mathcal{I}} h_m(\mathbf{x}_i - \mathbf{x}_o) r^{(k)}(\mathbf{x}_i) d\mathbf{x}_i \right. \\
&\quad \left. + [1 - a_m(z_o)] \int_{\mathcal{I}} h_{m+1}(\mathbf{x}_i - \mathbf{x}_o) r^{(k)}(\mathbf{x}_i) d\mathbf{x}_i \right\}, \quad \text{for } \mathbf{x}_o \in \mathcal{O}_m, \quad (11)
\end{aligned}$$

where

$$r^{(k)}(\mathbf{x}_i) = g(\mathbf{x}_i)/\hat{g}^{(k)}(\mathbf{x}_i)$$

and $m = 1, \dots, M$. Because the second convolution integral of the term inside the braces, $\{\}$, in Eq. (11) is used in the computation of stratum $m + 1$, evaluation of Eq. (11) requires $M + 1$ convolution operations and not $2M$ required for the computation of the forward model [Eq. (6)]. We have implemented all convolutions with fast Fourier transforms. Because of the wide spread of the PSF along the optical axis, padding in the axial direction was performed as we described previously⁴¹ for the EM algorithm. That is, the PSF was zero padded to twice the axial support of the estimated object function, and the latter was mirror replicated in the z axis to twice its original support.

It can be shown by mathematical induction that the estimates obtained by Eq. (11) are not stratified; i.e., they are continuous in z . To this end, let

$$d_m^{(k)}(\mathbf{x}_o) = \int_{\mathcal{I}} h_m(\mathbf{x}_i - \mathbf{x}_o) r^{(k)}(\mathbf{x}_i) d\mathbf{x}_i.$$

Then Eq. (11) can be written as:

$$\begin{aligned} \hat{s}^{(k+1)}(\mathbf{x}_o) &= \frac{\hat{s}^{(k)}(\mathbf{x}_o)}{H_M} \left\{ a_m(z_o) d_m^{(k)}(\mathbf{x}_o) + [1 - a_m(z_o)] d_{m+1}^{(k)}(\mathbf{x}_o) \right\} \\ &= \frac{\hat{s}^{(k)}(\mathbf{x}_o)}{H_M} \tilde{d}_m^{(k)}(\mathbf{x}_o) \quad \text{for } \mathbf{x}_o \in \mathcal{O}_m \end{aligned} \quad (12)$$

where

$$\tilde{d}_m^{(k)}(\mathbf{x}_o) = a_m(z_o) d_m^{(k)}(\mathbf{x}_o) + [1 - a_m(z_o)] d_{m+1}^{(k)}(\mathbf{x}_o) \quad \text{for } \mathbf{x}_o \in \mathcal{O}_m. \quad (13)$$

Assume that at iteration k , the specimen estimate $\hat{s}^{(k)}(\mathbf{x}_o)$ is continuous. Each of the projected ratios $d_m^{(k)}(\mathbf{x}_o)$ is a continuous function because it is the convolution

of $r^{(k)}(\mathbf{x}_i)$ with a smooth kernel (the space-invariant PSF $h_m(\cdot); m = 1, \dots, M + 1$). The update factor, $\tilde{d}_m^{(k)}(\mathbf{x}_o)$, in Eq. (12) is also continuous because it is calculated as a weighted average of two smooth functions, namely $d_m^{(k)}(\mathbf{x}_o)$ and $d_{m+1}^{(k)}(\mathbf{x}_o)$. As z_o approaches Z_m , $d_m^{(k)}(\mathbf{x}_o)$ bears more weight in the interpolation [Eq. (13)], whereas as z_o approaches Z_{m+1} , $d_{m+1}^{(k)}(\mathbf{x}_o)$ bears more weight in the interpolation. In general, there is a continuous transition from $z_o = Z_m$ to $z_o = Z_{m+1}$. Thus, the $k + 1$ iterate of the specimen function estimate is also continuous. If the initial guess is continuous (for example $\hat{s}^{(0)}(\mathbf{x}_o) = 1$ for all \mathbf{x}_o , which is a commonly-used initial guess for EM-based algorithms), it then follows that all iterates of the specimen estimate should also be continuous. For all the estimated results presented in Section 5, we used an initial estimate equal to 1 for all pixels.

Eq. (11) yields an iterative depth-variant EM (DV-EM) algorithm for ML image estimation based on an approximate imaging model. As mentioned earlier, the approximation in the imaging model improves as the number of PSFs (or strata) increases at the expense of increased computation time. Thus, the number of strata [Eq. (2)] regulates the trade-off between the computation time and the quality of the estimated specimen function.

The algorithm as well as the synthetic data generation described in the next section were implemented using the C programming language and run on an Origin 2100 computer (Silicon Graphics, Inc., Mountain View, CA) equipped with four R12000/330-MHz processors and a 5-Gbyte RAM.

4. Experimental Methods

A. Synthetic Data

We evaluated the stratum-based model for depth-varying image formation and the restoration algorithm using synthetic images of numerically-generated test objects. This has the advantage that the actual object function is exactly known, and thus the quality of the estimated object function can be readily assessed. We generated the synthetic images with Eq. (6) using five planes per stratum. For the different PSFs we assumed a $60\times/1.4$ N.A. oil-immersion objective with oil of refractive index equal to 1.515. We computed the PSFs using the program in our XCOSM v2.5 package³¹ for a fluorescent wavelength equal to 530 nm at specified depths in a specimen with mounting medium different than oil. For all test objects discussed below, zero depth coincides with the location of the cover slip (i.e. the top of the object directly on the cover slip) and depth increases below the cover slip along the optical axis. Unless otherwise noted, we assumed that the mounting medium of the test objects is water (refractive index, $n_w = 1.33$) which is typical for many live biological specimens.

The first numerically-generated test object consists of three small spheres ($0.45 \mu\text{m}$ in diameter) centered at depths $0.225 \mu\text{m}$, $1.125 \mu\text{m}$, and $2.025 \mu\text{m}$ on a $128 \times 128 \times 128$ grid with voxels of size $0.09 \mu\text{m}^3$ (Fig. 1a). The spheres are centered in each plane of the 3D image. For the forward model, we used six PSFs computed at depths of $0.45 \mu\text{m}$ apart. We used this test object along with three simpler test objects (with the same grid and voxel size) each of which consisted of a single sphere positioned at a different depth along the optical axis in order to demonstrate the depth-variant

stratum-based model and the effect of the changing PSF due to imaging depth. The images of the single-sphere objects were obtained by the 3D convolution of each test object with the appropriate PSF at each depth.

The second test object is a single 4- μm in diameter sphere positioned at zero depth on a $256 \times 256 \times 256$ grid with voxels of size $0.06 \mu\text{m}^3$. For the forward model, we used 15 PSFs computed at depth increments of $0.3 \mu\text{m}$ assuming that the refractive index of the mounting medium of the object is equal to 1.4. This refractive index was assumed in order to match a real phantom specimen (described in Section 4 B), which we imaged in order to evaluate our model (Fig. 2).

B. Measured Data

We recorded a 3D image of a 4- μm in diameter fluorescent microsphere (TetraSpec Kit T-14792, Molecular Probes, Inc., Eugene, OR) with a Nikon Eclipse TE200 equipped with a charged-couple device (CCD) camera (Photometrics Quantix 57, Roper Scientific) with 535×512 pixels and well size equal to $13 \mu\text{m} \times 13 \mu\text{m}$. We used an infinity corrected Plan Apo $60 \times / 1.4$ N.A. oil-immersion objective lens, with a 0.21 mm working distance, and a $2 \times$ Optivar relay lens yielding an effective square pixel with size of $0.12 \mu\text{m}^2$ in the image. The step size between focal planes was set to $0.12 \mu\text{m}$. The refractive index of the immersion oil used is 1.5150. Excitation and emission filters centered at 490 nm and 530 nm with full-width at half maximum of 20 nm and 30 nm respectively, were used. The microsphere, stained with four different fluorescent dyes, is mounted in an optical cement with refractive index $n = 1.4$.

C. Comparison of Measured and Synthetic Data

We first generated synthetic data with higher resolution than the measured data using PSFs sampled at a rate higher than the Nyquist spatial-sampling rate for the 60×1.4 N.A. oil-immersion objective lens. Then, to compare to measured data and mimic the integration over a CCD well that occurs in practice, we averaged an appropriate number of adjacent pixels in the synthetic data to match the lower resolution of the measured data. To permit quantitative comparison of the data, we generated xz sections from the 3D images containing the peak intensity and then scaled each section so that the sections' integrated intensities were equal. We displayed images of measured and synthetic data by normalizing intensities to the interval $[0,1]$.

D. Image Restoration and Performance Measures

For the evaluation of the restoration algorithm, we reduced the size of the simulations from three dimensions (x, y, z) , to two dimensions (x, z) , without loss of generality, by using the line-spread function (LSF), $f(x, z)$, of the microscope given by:

$$f(x, z) = \int_{-\infty}^{\infty} h(x, y, z) dy,$$

where $h(x, y, z)$ is the PSF. For the forward model and the restoration we used the same number of LSFs computed from PSFs defined at depth increments of $0.3 \mu m$ apart. The test object consists of two small discs ($0.36 \mu m$ in diameter) centered at depths $0.18 \mu m$ and $1.04 \mu m$ on a 128×128 grid with square pixels of size $0.06 \mu m^2$. For this 2-disc object we used 6 LSFs.

We also used an annulus test object with an outer diameter of approximately 2.4

μm and a thickness of $0.6 \mu\text{m}$ on a 128×128 grid with square pixels of size $0.06 \mu\text{m}^2$. For the annulus object we used 8 LSFs.

Image restoration with the EM algorithm in our XCOSM v2.5 package,³¹ which we denote as the space-invariant EM (SI-EM) algorithm, was performed using a single LSF computed from the PSF defined at a zero depth because this is the PSF used routinely in COSM image restoration. For the annulus test object, we also used an LSF computed from the PSF defined at depth of $1.2 \mu\text{m}$ which coincides with the center of the annulus. To compare the performance of the DV-EM and SI-EM algorithms, we used in the simulations the same synthetic data, generated with the depth-variant model and multiple (5 or 8 depending on the test object) LSFs as defined above.

For the evaluation of the restoration algorithms we compared the estimated object, $\hat{\mathbf{s}}$, to the true object, \mathbf{s} , at each iteration using Csiszar's I-divergence⁴² (IDIV) discrepancy measure given by:

$$\text{IDIV} = \sum_{i=1}^J (s_i \ln \frac{s_i}{\hat{s}_i} + \hat{s}_i - s_i), \quad (14)$$

where J is the total number of pixels in the true and estimated objects.

The ability to resolve the two discs in the restoration of the second object was quantified with an average visibility (\mathcal{V}) computed at each iteration and given by

$$\mathcal{V} = \frac{\bar{s}_b - \bar{d}}{\bar{s}_b + \bar{d}} \quad (15)$$

where \bar{s}_b is the average pixel value in 3×3 -pixels areas in the estimated object centered at the center of the discs in the actual test object, and \bar{d} is the average pixel value in a 3×3 -pixels area of the estimated object centered halfway between the centers of the discs along the optical axis, z .

5. Results

A. Model evaluation

To test the depth-variant stratum-based model presented in Section 2, we first generated the image of a 3-sphere test object (Figure 1a) as described in Section 4 A. Because the 3-sphere object is the superposition of three single-sphere objects, we compared the image of the 3-sphere object (Figure 1b) to the superposition of the images of the three single-sphere objects (Figure 1c, d, and e) and found good agreement. The asymmetry along the z axis in the images in Figure 1b, d, and e is due to spherical aberration. The image in Figure 1c is symmetric along the z axis because it was generated with the aberration-free PSF defined at zero depth, which coincides with the top of the sphere in this case.

For the evaluation of the depth-variant imaging model we compare in Figure 2 a measured image of a $4\text{-}\mu\text{m}$ bead phantom (see Section 4 B) to a model prediction generated as described in Section 4 A. Profiles along the z axis through the center of the images are also plotted in Figure 2. As evident from this figure the depth-variant model captures the major feature in the measured image of the bead, i.e. the asymmetry along the optical axis caused by spherical aberration introduced by the refractive-index mismatch.

B. DV-EM algorithm evaluation

Figure 3 shows images of the true annulus-test-object; its simulated image predicted by the depth-variant model; and the object estimates computed with the DV-EM algorithm derived in Section 3 and the SI-EM algorithm in our XCOSM v2.5 package.³¹

This figure indicates that if depth-variance is not taken into account in the restoration algorithm, the algorithm produces a very artifactual object estimate (Figure 3e, f, g, and h) whereas the DV-EM produces a result that resembles the test object well (Figure 3c and d). Vertical profiles through the middle of the images along the z axis (Figure 4) provide a quantitative comparison of these results. Using the single-valued I-divergence discrepancy measure described in Section 4, we compare the object intensity estimated by the two algorithms to the true object intensity. Figure 5 plots the IDIV measure [Eq. (14)] versus iteration number for the DV-EM and SI-EM algorithms. As evident from this figure, the two algorithms yield different results after 25 iterations. The SI-EM algorithm yields an estimate that deviates from the actual specimen function as evidenced by the increasing IDIV after about 90 iterations. With the DV-EM, on the other hand, the IDIV keeps decreasing, albeit slowly, up to at least 10^5 iterations. This slow convergence rate is known to be intrinsic to the EM algorithm, regardless of whether the PSF is shift varying or not.^{7,41}

Similar results were obtained for the 2-disc object and are summarized in Figures 6 to 9. Profiles through the estimated images (Figure 6c, e, and g) show that the two discs are resolved (Figure 7) but artifacts are evident in the image obtained with SI-EM: the position of the discs is incorrect and a third peak is evident (Figure 6d, f, and h). The IDIV and visibility measures computed at each iteration of the two algorithms are plotted in Figures 8 and 9 respectively.

6. Summary and Conclusions

Using the expectation maximization formalism we have developed a new algorithm for maximum-likelihood image restoration based on a depth-variant model for image formation. The model, presented in this paper, takes into account a depth-variant PSF, i.e. a PSF that changes with imaging depth due to spherical aberration caused by the refractive-index mismatch between the immersion medium of the objective lens and the mounting medium of the specimen.

To reduce the complexity of the image formation model and algorithm, we segment the axial support of the object space into a small number of strata. The PSFs at the top and bottom of each stratum are associated with all the planes in the stratum. Thus, this stratum-based approach yields an approximate model that allows a significant reduction in the number of PSFs needed for the depth-variant image estimation. The accuracy in the model for image formation improves as the number of strata (and thus the number of PSFs) increases. However, the computation time and memory requirements also increase with the number of strata. Thus, the number of strata regulates the trade-off between the computation time and the quality of the estimated specimen function.

Simulated images of a 4 μm in diameter fluorescent microsphere obtained with our approximate model are similar to images of such a microsphere recorded from the microscope. Results obtained from simulations show that the depth-variant EM algorithm can compensate for the depth varying spherical aberration in the synthetic data whereas the EM algorithm derived on a space-invariant model produces artifac-

tual estimates. Future work includes further evaluation of the model using different phantom specimens and investigation of the trade-off regulated by the number of strata used in the image estimation.

Based on our results, we conclude that existing COSM restoration algorithms, derived from a space-invariant imaging model, cannot fully compensate for the image degradation introduced by spherical aberration due to imaging depth. The work presented in this paper is the first step towards depth-variant image estimation for optical-sectioning microscopy.

Acknowledgments

This work was supported by the National Institutes of Health grants RO1 GM55708 and 5R01 GM4979808.

J.-A. Conchello can be reached at the address on the title page; by telephone at 405-271-6137, by fax at 405-271-3153, or by e-mail at jose-conchello@omrf.ouhsc.edu.

References

1. C. Preza, M. I. Miller, L. J. Thomas, Jr., and J. G. McNally, “Regularized Linear Method for Reconstruction of Three-Dimensional Microscopic Objects From Optical Sections,” *J. Opt. Soc. Am. A*, **9**, 219–228 (1992).
2. C. Preza, M. I. Miller, and J.-A. Conchello, “Image Reconstruction for 3-D Light Microscopy With a Regularized Linear Method Incorporating a Smoothness Prior,” in *Biomedical Image Processing and Biomedical Visualization*, R. S. Acharya and D. B. Goldgof, eds., Proc. SPIE **1905**, 129–139 (1993).

3. J.-A. Conchello, J. J. Kim, and E. W. Hansen, “Enhanced 3-D Reconstruction From Confocal Scanning Microscope Images. 2: Depth Discrimination vs Signal-to-Noise Ratio in Partially Confocal Images ,” *Appl. Opt.* , **33**, 3740–3750 (1994).
4. J.-A. Conchello, “Super-resolution and point-spread function sensitivity analysis of the expectation-maximization algorithm for computational optical sectioning microscopy,” in *Image Reconstruction and Restoration*, T. J. Schulz, ed., Proc. SPIE **2302**, 369–378 (1994).
5. J.-A. Conchello and J.G. McNally, “Fast regularization technique for expectation maximization algorithm for computational optical sectioning microscopy,” in *Proceedings of the IS&T/SPIE symposium on Electronic Imaging, Science and Technology*, C. J. Cogswell, G. S. Kino, and T. Wilson, eds., **2655**, 199–208 (1996).
6. Markham J. and J.-A. Conchello, “Tradeoffs in regularized maximum-likelihood image restoration,” in *Three-Dimensional Microscopy: Image Acquisition and Processing IV*, C. J. Cogswell, J.-A. Conchello, and T. Wilson, eds., Proc. SPIE **2984**, 136–145 (1997).
7. Markham J. and J.-A. Conchello, “Fast maximum-likelihood image-restoration algorithms for three-dimensional fluorescence microscopy,” *J. Opt. Soc. Am. A*, **18**, 1062–1071, (2001).
8. D.A. Agard, “Optical Sectioning Microscopy,” *Annual Review of Biophysics and Bioengineering*, **13**, 191–219, (1984).
9. D.A. Agard, Y. Hiraoka, P. Shaw, and J.W. Sedat, “Fluorescence Microscopy in Three Dimensions,” *Methods in Cell Biology*, **30**, 353–377 (1989).

10. A. Erhardt, G. Zinser, D. Komitowski, and J. Bille, “Reconstructing 3-D Light-Microscopic Images by Digital Image Processing,” *Appl. Opt.* , **24**, 194–200 (1985).
11. T. J. Holmes, “Maximum-Likelihood Image Restoration Adapted For Noncoherent Optical Imaging,” *J. Opt. Soc. Am. A*, **5**, 666 – 673 (1988).
12. T. J. Holmes, “Expectation-maximization Restoration of Band-limited, Truncated Point-Process Intensities with Application in Microscopy,” *J. Opt. Soc. Am. A*, **6**, 1006 – 1014 (1989).
13. W. A. Carrington, K. E. Fogarty, and F. S. Fay, 3D fluorescence imaging of single cells using image restoration, in *Noninvasive Techniques in Cell Biology*, J. K. Fosket and S. Grinstein, eds. (Wiley-Liss, New York, 1990), pp. 53–72.
14. W. A. Carrington, E. D. Lynch, W. Moore, G. Isenberg, K. E. Fogarty, and F. S. Fay, “Superresolution three-dimensional images of fluorescence in cells with minimal light exposure,” *Science*, **268**, 1483–1487 (1995).
15. S. Joshi and M. I. Miller, “Maximum *a posteriori* Estimation with Good’s Roughness for Optical-Sectioning Microscopy,” *J. Opt. Soc. Am. A*, **10**, 1078–1085 (1993).
16. P.J. Verveer and T. M. Jovin, “Efficient superresolution restoration algorithms using maximum *a posteriori* estimation with application to fluorescence microscopy,” *J. Opt. Soc. Am. A*, **14**, 1696–1706 (1997).
17. P.J. Verveer, M. J. Gemkow, and T. M. Jovin, “A comparison of image restoration approaches applied to three-dimensional confocal and wide-field fluorescence

- microscopy ,” *J. of Microscopy*, **193**, 50–61 (1999).
18. S. S. Stefanou and E. W. Hansen, “Restoration of edges under Poisson noise using convex constraints with application to 3D optical microscopy,” in *Three-Dimensional Microscopy: Image Acquisition and Processing IV*, C. J. Cogswell, J.-A. Conchello, and T. Wilson, eds., Proc. SPIE **2984**, 232–242 (1997).
 19. Z. Kam, B. Hanser, M. G. L. Gustafsson, D. A. Agard, and J.W. Sedat, “Computational adaptive optics for live three-dimensional biological imaging,” *Proceedings of the National Academy of Science*, **98**, 3790–3795 (2001).
 20. J. B. Pawley, “Limitations on optical sectioning in live-cell confocal microscopy,” *Scanning*, **24**, 241-246 (2002).
 21. S. F. Gibson and F. Lanni, “Experimental Test of an Analytical Model of Aberration in an Oil-Immersion Objective Lens Used in Three-Dimensional Light Microscopy,” *J. Opt. Soc. Am. A*, **9**, 154–66 (1992).
 22. L. R. Sherman, O. Albert, C. F. Schmidt, G.V. Vdovin, G. A. Mourou, and T. B. Norris, “Adaptive compensation for aberrations in ultrafast three dimensional microscopy using a deformable mirror,” in *Three-Dimensional and Multidimensional Microscopy: Image Acquisition and Processing VII*, J.-A. Conchello, C. J. Cogswell, and T. Wilson, eds., Proc. SPIE **3919**, 9–13 (2000).
 23. L. Sherman, J. Y. Ye, O. Albert, T. B. Norris, “Adaptive correction of depth-induced aberrations in multiphoton scanning microscopy using a deformable mirror,” in *J. of Microscopy-Oxford*, **206**, 65–71 (2002).
 24. M. J. Booth, M. A. A. Neil, R. Juskaitis, T. Wilson, “Adaptive aberration cor-

- rection in a confocal microscope,” in *Proceedings of the National Academy of Sciences of the United States of America*, **99**, 5788–5792 (2002).
25. P. N. Marsh, D. Burns, J. M. Girkin, “Practical implementation of adaptive optics in multiphoton microscopy,” in *Optics Express*, **11**, 1123–1130, (2003).
 26. S. F. Gibson and F. Lanni, “Measured and analytical point spread functions of the optical microscope for use in 3-D optical serial sectioning microscopy,” in *Optical Microscopy for Biology* (Wiley-Liss, Inc., New York, 1990).
 27. H. Leung, “The importance of mounting medium’s refractive index and cover glass thickness for reducing optical aberrations on confocal laser scanning microscope (CLSM) ,” *Microscopical Society of Canada Bullentin*, **21**, 19–24 (1993).
 28. J. G. McNally, C. Preza, J.-A. Conchello, and L. J. Thomas, Jr, “Artifacts in Computational Optical-Sectioning Microscopy ,” *J. Opt. Soc. Am. A*, **11**, 1056–1067, (1994).
 29. A. D. Dempster, N. M. Laird, and D. B. Rubin, “Maximum Likelihood From Incomplete Data via the EM Algorithm,” *J. Royal Statistical Society, B*, **39**, 1–37 (1977).
 30. J.-A. Conchello and E. W. Hansen, “Enhanced 3-D Reconstruction From Confocal Scanning Microscope Images. 1: Deterministic and Maximum Likelihood Reconstructions,” *Appl. Opt.* , **19**, 3795–3804 (1990).
 31. The XCOSM deconvolution package is available at:
<http://3Dmicroscopy.wustl.edu/xcosm>.
 32. M. Faisal, A. D. Lanterman, D. L. Snyder, and R. L. White, “Implementation of

- a modified Richardson-Lucy method for image restoration on a massively parallel computer to compensate for space-variant point spread of a charge-coupled-device camera ,” *J. Opt. Soc. Am. A*, **12**, 2593–2603 (1995).
33. A. F. Boden, D. C. Redding, R. J. Hanisch, and J. Mo, “Massively parallel spatially variant maximum-likelihood restoration of Hubble Space Telescope imagery ,” *J. Opt. Soc. Am. A*, **13**, 1537–1545 (1996).
 34. J. G. Nagy and D. P. O’Leary, “Restoring Images Degraded by Spatially Variant Blur ,” *SIAM J. Sci. Comput.*, **19**, 1063–1082 (1998).
 35. H.J. Trussell and B. R. Hunt, “Image Restoration of Space-Variant Blurs by Sectioned Methods ,” *IEEE Transactions on Acoustics, Speech, and Signal Processing*, **ASSP-26**, 608–609 (1978).
 36. J. G. Nagy, V. P. Pauca, R. J. Plemmons, T. C. Torgersen, “Space-varying restoration of optical images ,” *J. Opt. Soc. Am. A* , **14**, 3162–3174 (1997).
 37. C. Preza and J.-A. Conchello, “Image estimation accounting for point-spread function depth variation in three-dimensional fluorescence microscopy,” in *Three-Dimensional Microscopy: Image Acquisition and Processing X*, J.-A. Conchello, C. J. Cogswell, and T. Wilson, eds., Proc. SPIE **4964**, 135–142 (2003).
 38. D. E. Dudgeon and R.M. Mersereau, *Multidimensional Digital Signal Processing* (Prentice-Hall, Inc., New Jersey, 1984).
 39. G. M. P. van Kempen, L.J. van Vliet, P.J. Verveer, and H.T.M van der Voort, “A quantitative comparison of image restoration methods for confocal microscopy ,” *J. of Microscopy*, **185**, 354–365 (1994).

40. D.L. Snyder and M. I. Miller, *Random Point Processes in Time and Space* (Springer-Verlag, New York, 1991).
41. J.-A. Conchello, “Superresolution and convergence properties of the expectation-maximization algorithm for maximum-likelihood deconvolution of incoherent images,” *J. Opt. Soc. Am. A*, **15**, 2609–2619 (1998).
42. I. Csiszár, “Why Least Squares and Maximum Entropy? An Axiomatic Approach to Inference for Linear Inverse Problems,” *Annals of Statistics*, **19**, 2032–2066 (1991).

List of Figure Captions

Fig. 1. xz -section images through the center of: (a) the 3-sphere test object; (b) the image of the 3-sphere object with a $60\times/1.4$ N.A. oil-immersion lens predicted by the depth-variant stratum-based model; and images of single-sphere test objects with the sphere centered at depth $0.225\ \mu\text{m}$ (c), $1.125\ \mu\text{m}$ (d), and $2.025\ \mu\text{m}$ (e) below the cover slip, obtained by the convolution of each test object with the appropriate PSF at each depth. The spheres have a diameter equal to $0.45\ \mu\text{m}$. prezaF2.eps.

Fig. 2. Comparison of xz -section images through the center of a measured image (left) and a simulated image (right) of the $4\text{-}\mu\text{m}$ bead phantom. Profiles through the center of the images are shown in the bottom panel. prezaF2top.eps and prezaF2bottom.eps

Fig. 3. xz -images of the true (a) and the estimated annulus object computed from the synthetic image (b) with: the DV-EM algorithm after 100,000 iterations (c), and after 20,000 iterations (d); and the SI-EM algorithm using an LSF defined at a depth of $0\ \mu\text{m}$ (e and f) and $1.2\ \mu\text{m}$ (g and h) after 100,000 iterations (e and g), and after 20,000 iterations (f and h). The size of the images shown is 96×96 pixels. prezaF3.eps.

Fig. 4. Vertical profiles through the middle of xz -section images of the annulus test object (Truth) and the estimated images computed with the DV-EM algorithm after a different number of iterations (20k and 100k) shown in Figure 3(a, c, and d). prezaF4.eps

Fig. 5. I-divergence (IDIV) discrepancy measure between the true and estimated object computed at each iteration of the DV-EM algorithm and the SI-EM algorithm for the annulus test object. For the SI-EM algorithm, results are shown obtained with

a single LSF defined at a depth of $0 \mu\text{m}$ (0) and $1.2 \mu\text{m}$ (1.2). The x axis is displayed on a logarithmic scale. prezaF5.eps.

Fig. 6. xz -images of the true (a) and the estimated 2-disc object computed from the synthetic image (b) with the DV-EM (left) and the SI-EM algorithm (right) after 50,000 DV-EM iterations (c), 50,000 SI-EM iterations (d), 10,000 DV-EM iterations (e), 10,000 SI-EM iterations (f), 2,000 DV-EM iterations (g), and 2,000 SI-EM iterations. The size of the images shown is 64×64 pixels. prezaF6.eps

Fig. 7. Vertical profiles through the middle ($x = 1.74 \mu\text{m}$) of the xz -section images of the 2-disc object (Truth) and the estimated images computed with the DV-EM algorithm after a different number of iterations (2k, 10k, and 50k) shown in Figure 6(a, c, e, and g). prezaF7.eps

Fig. 8. I-divergence (IDIV) discrepancy measure between the true and estimated object computed at each iteration of the DV-EM algorithm and the SI-EM algorithm for the 2-disc test object. The x axis is displayed on a logarithmic scale. prezaF8.eps.

Fig. 9. Visibility measure computed at each iteration of the DV-EM algorithm and the SI-EM algorithm for the 2-disc test object. prezaF9.eps.

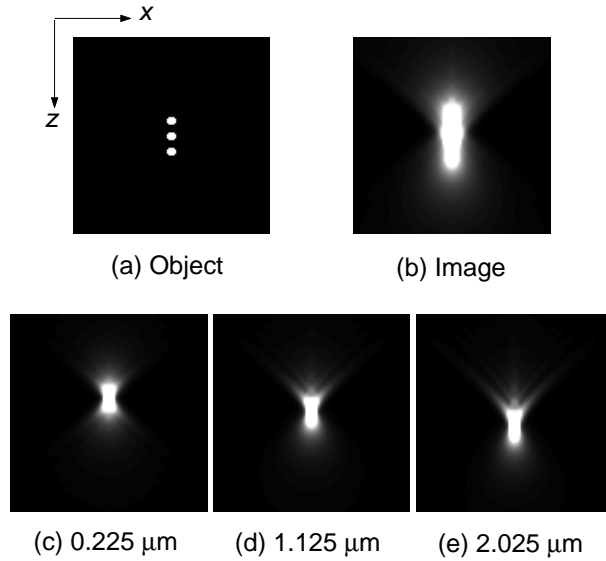


Fig. 1. xz -section images through the center of: (a) the 3-sphere test object; (b) the image of the 3-sphere object with a $60\times/1.4$ N.A. oil-immersion lens predicted by the depth-variant stratum-based model; and images of single-sphere test objects with the sphere centered at depth $0.225\ \mu m$ (c), $1.125\ \mu m$ (d), and $2.025\ \mu m$ (e) below the cover slip, obtained by the convolution of each test object with the appropriate PSF at each depth. The spheres have a diameter equal to $0.45\ \mu m$. prezaF1.eps.

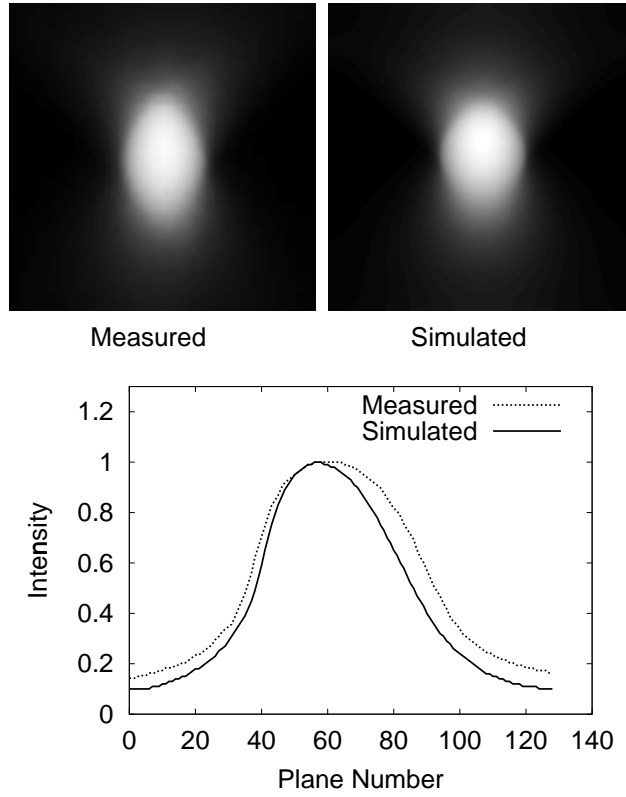


Fig. 2. Comparison of xz -section images through the center of a measured image (left) and a simulated image (right) of the $4\text{-}\mu\text{m}$ bead phantom. Profiles through the center of the images are shown in the bottom panel.

prezaF2top.eps and prezaF2bottom.eps

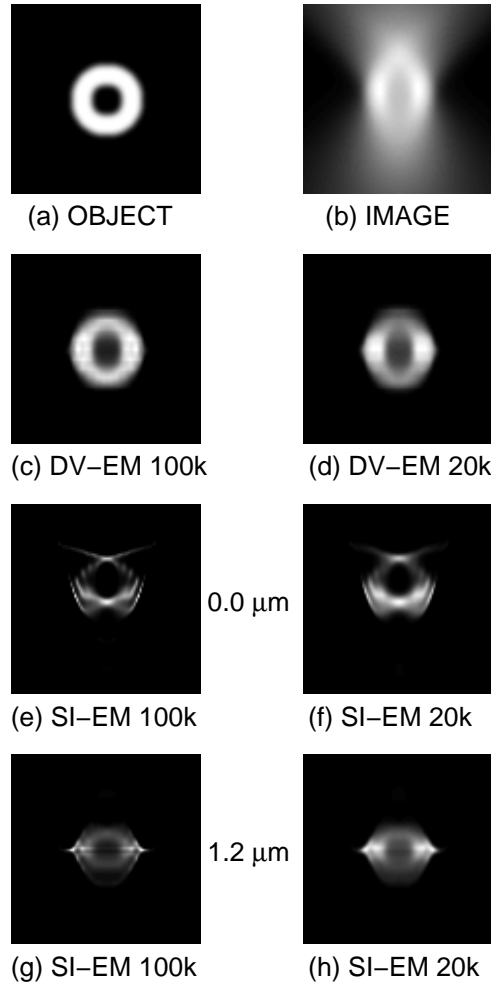


Fig. 3. xz -images of the true (a) and the estimated annulus object computed from the synthetic image (b) with: the DV-EM algorithm after 100,000 iterations (c), and after 20,000 iterations (d); and the SI-EM algorithm using an LSF defined at a depth of $0 \mu\text{m}$ (e and f) and $1.2 \mu\text{m}$ (g and h) after 100,000 iterations (e and g), and after 20,000 iterations (f and h). The size of the images shown is 96×96 pixels. prezaF3.eps.

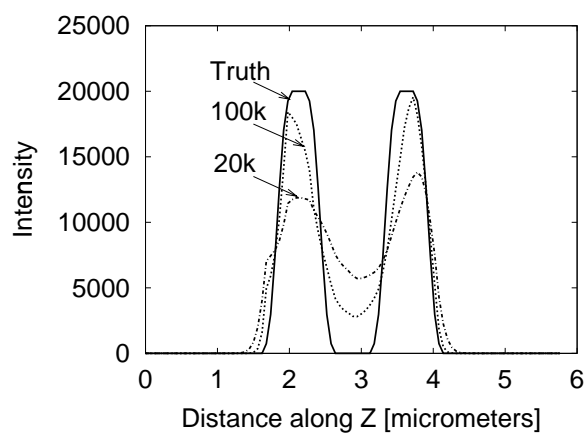


Fig. 4. Vertical profiles through the middle of xz -section images of the annulus test object (Truth) and the estimated images computed with the DV-EM algorithm after a different number of iterations (20k and 100k) shown in Figure 3(a, c, and d). prezaF4.eps

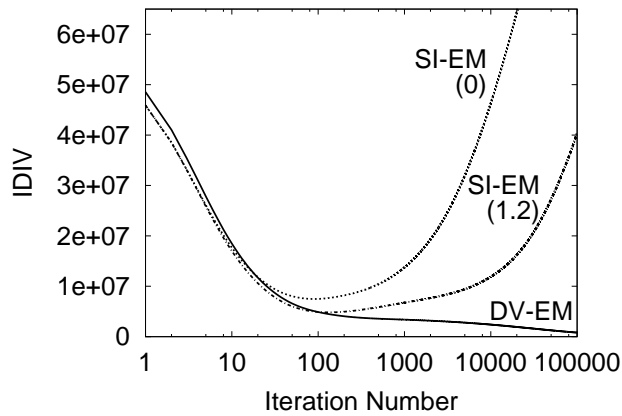


Fig. 5. I-divergence (IDIV) discrepancy measure between the true and estimated object computed at each iteration of the DV-EM algorithm and the SI-EM algorithm for the annulus test object. For the SI-EM algorithm, results are shown obtained with a single LSF defined at a depth of $0 \mu\text{m}$ (0) and $1.2 \mu\text{m}$ (1.2). The x axis is displayed on a logarithmic scale. prezaF5.eps.

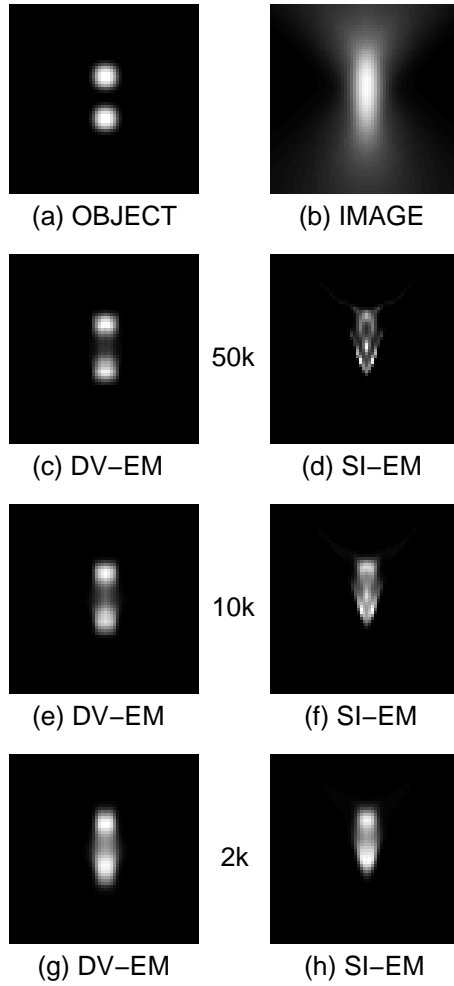


Fig. 6. xz -images of the true (a) and the estimated 2-disc object computed from the synthetic image (b) with the DV-EM (left) and the SI-EM algorithm (right) after: 50,000 DV-EM iterations (c); 50,000 SI-EM iterations (d); 10,000 DV-EM iterations (e); 10,000 SI-EM iterations (f); 2,000 DV-EM iterations (g); and 2,000 SI-EM iterations (h). The size of the images shown is 64×64 pixels.

prezaF6.eps

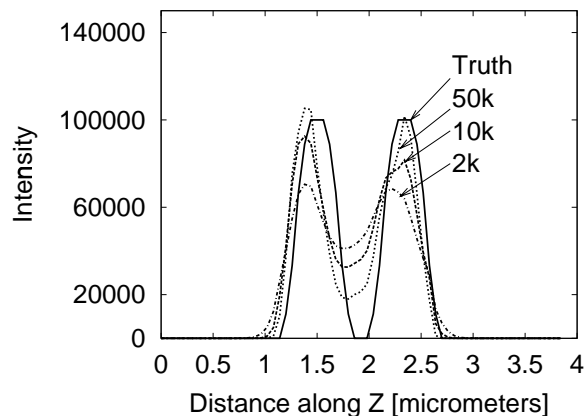


Fig. 7. Vertical profiles through the middle ($x = 1.74 \mu m$) of the xz -section images of the 2-disc object (Truth) and the estimated images computed with the DV-EM algorithm after a different number of iterations (2k, 10k, and 50k) shown in Figure 6(a, c, e, and g). prezaF7.eps

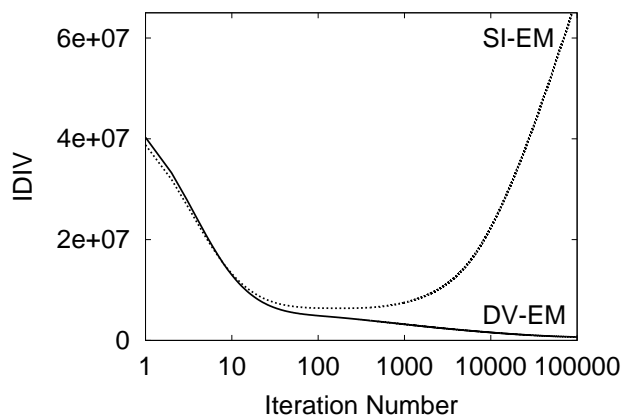


Fig. 8. I-divergence (IDIV) discrepancy measure between the true and estimated object computed at each iteration of the DV-EM algorithm and the SI-EM algorithm for the 2-disc test object. The x axis is displayed on a logarithmic scale. prezaF8.eps.

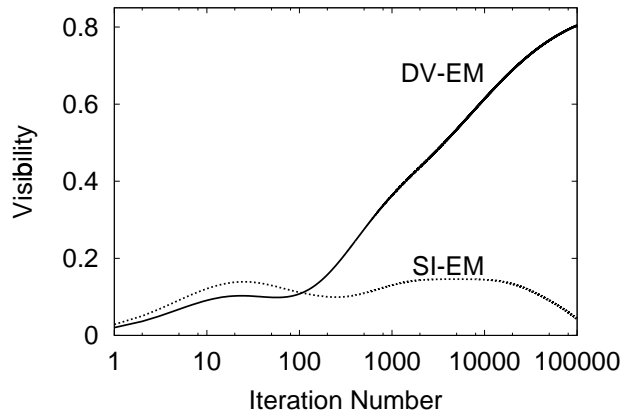


Fig. 9. Visibility measure computed at each iteration of the DV-EM algorithm and the SI-EM algorithm for the 2-disc test object. prezaF9.eps.